1   **Neuroglia Infection by Rabies Virus after Anterograde Virus Spread in Peripheral Neurons**

2

3   Madlin Potratz, Luca M. Zaeck, Carlotta Weigel, Antonia Klein, Conrad M. Freuling, Thomas Müller, Stefan

4   Finke*

5   *Friedrich-Loeffler-Institut (FLI), Federal Research Institute for Animal Health, Institute of Molecular Virology*

6   *and Cell Biology, 17493 Greifswald-Insel Riems, Germany*

7

8

9

10   * Correspondence: stefan.finke@fli.de; Tel.: +49-38351-71283; Fax.: +49-38351-71151

11

12

13

14

15

18

Abstract

The highly neurotropic rabies virus (RABV) enters peripheral neurons at axon termini and requires long distance axonal transport and trans-synaptic spread between neurons for the infection of the central nervous system (CNS). Whereas laboratory strains are almost exclusively detected in neurons, recent 3D imaging of field RABV-infected brains revealed an remarkably high proportion of infected astroglia, indicating that in contrast to attenuated lab strains highly virulent field viruses are able to suppress astrocyte mediated innate immune responses and virus elimination pathways. While fundamental for CNS invasion, *in vivo* field RABV spread and tropism in peripheral tissues is understudied. Here, we used three-dimensional light sheet and confocal laser scanning microscopy to investigate the *in vivo* distribution patterns of a field RABV clone in cleared high-volume tissue samples after infection via a natural (intramuscular; hind leg) and an artificial (intracranial) inoculation route. Immunostaining of virus and host markers provided a comprehensive overview of RABV infection in the CNS and peripheral nerves after centripetal and centrifugal virus spread. Importantly, we identified non-neuronal**,** axon-ensheathing neuroglia (Schwann cells, SCs) in peripheral nerves of the hind leg and facial regions as a target cell population of field RABV. This suggest that virus release from axons and infected SCs is part of the RABV *in vivo* cycle and may affect RABV-related demyelination of peripheral neurons and local innate immune responses. Detection of RABV in axon surrounding myelinating SCs after i.c. infection further provided evidence for anterograde spread of RABV, highlighting that RABV axonal transport and spread of infectious virus in peripheral nerves is not exclusively retrograde. Our data support a new model in which, comparable to CNS neuroglia, SC infection in peripheral nerves suppresses glia-mediated innate immunity and delays antiviral host responses required for successful transport from the peripheral infection sites to the brain.

41   **Introduction**

42   Rabies is estimated to cause 59.000 human deaths annually in over 150 countries, with 95% of cases occurring in

43   Africa and Asia (reviewed in [26,21]). The disease is caused by a plethora of highly neurotropic, non-segmented,

44   single-stranded RNA viruses of negative polarity belonging to the family *Rhabdoviridae* of the order

45   *Mononegavirales,* of which the rabies virus (RABV) is the type species of the Lyssavirus genus [2]. RABV and

46   other lyssaviruses enter the nervous system at the synapses of peripheral neurons. After receptor-mediated

47   endocytosis, the virions remain in endosomal vesicles and hijack the retrograde axonal transport machinery

48   [33,23,59] to reach the neuron soma, where virus ribonucleoproteins (RNPs) are released into the cytoplasm [47]

49   for virus gene expression and replication. Newly formed virus is then transported to post-synaptic membranes,

50   followed by trans-synaptic spread to connected neurons [12]. Prolonged replication of pathogenic RABV in the

51   brain eventually leads to the onset of a progressive rabies encephalitis, invariably resulting in the fatal disease

52   progression. In animals suffering from RABV encephalitis, the virus can be detected in multiple nervous or

53   innervated tissues including hind leg, spinal cord, brain, face, and salivary glands [5,15]. For the transmission of

54   infectious virus to new hosts via virus-containing saliva, centrifugal spread of RABV in the peripheral nervous

55   system (PNS) is required [18]. The secretion of RABV-containing saliva by salivary glands is commonly accepted

56   as the main source of virus shedding and virus transmission to uninfected animals via bites (reviewed in [21,16]).

57   Detection of RABV in sensory neurons of the olfactory epithelium and other tissues during late stages of infection

58   indicates that, at least in these late phases of disease, the axonal transport is not exclusively retrograde (reviewed

59   in [16]). In fact, studies have shown that RABV enters the anterograde axonal transport pathway in cultivated

60   primary rat dorsal root ganglion (DRG) neurons [6] and in mice [70]. However, the consequences of anterograde

61   transport of RABV is still controversially discussed, even though infection through intradermal sensory neurons

62   represents a likely route of entry for lyssaviruses as a result from bat bites [7].

63   Because of their trans-synaptic spread, RABVs constitute ideal viruses to map neuronal connections [67,66] as

64   even attenuated RABVs enter axonal transport pathways [33]. More neuroinvasive yet still lab-adapted strains like

65   CVS-11 have been used as polysynaptic neuron tracers and the resultant insights have subsequently been used to

66   explain *in vivo* RABV spread and pathogenesis [61]. However, already between different CVS strains, substantial

67   differences in pathogenicity exist [39], raising the question whether knowledge from established lab-adapted

68   strains can be extrapolated to explain actual field RABV infection and pathogenesis.

69   The advent of efficient full-genome cloning techniques opened novel avenues for the analysis of virus variability

70   in combination with phenotypical characterization of recombinant field viruses at a clonal level [43]. For example,

71   a recent comparison of field and lab RABV clones in mice revealed that field viruses not only showed a higher

3

72   virulence compared to lab strains such as CVS-11 but also substantially differ in their ability to establish infection

73   in non-neuronal astroglia in the central nervous system (CNS) [48]. In contrast to attenuated lab-adapted RABV,

74   which is supposed to be eliminated from infected glial cells (astrocytes) by type I interferon-induced immune

75   reactions [46], it has been hypothesized that rapid onset of field virus gene expression in non-neuronal astrocytes

76   blocks inhibitory innate immune activation and responses [48]. This may not only affect RABV replication in glial

77   cells directly but also in surrounding neurons via paracrine signalling. Thus, this mechanism may be crucial to

78   RABV spread and pathogenesis *in vivo*. Apart from astrocytes, *in vivo* infection of non-neuronal muscle,

79   epidermal, and epithelial cells have been described [12,5,13,42]. In foxes, which had been orally immunized with

80   live-attenuated RABV, infected cells can be detected in the epithelium of lymphoid tonsils [63,56]. *In vitro*, even

81   immature DCs or monocytes can be infected [35]. Overall, knowledge on the broad spectrum infection pattern of

82   RABV *in vivo,* particularly of field RABV strains, is still incomplete and the identification of PNS and non-

83   neuronal cells involved in RABV spread and pathogenesis has been given little attention.

84   Therefore, by using a highly virulent field RABV clone of dog origin (rRABV Dog) [43], we set out to

85   systematically and comprehensively elucidate the *in vivo* spread and cell tropism of a field RABV strain. So far,

86   technical limitations in conventional histology to visualize infection processes in complex tissues in large three-

87   dimensional (3D) volumes at a mesoscopic scale and high resolution hindered a comprehensive overview of RABV

88   cell tropism, *in vivo* spread, and pathogenesis. Immunofluorescence-compatible tissue clearing iDISCO and

89   uDISCO (immunolabeling-enabled and ultimate three-dimensional imaging of solvent-cleared organs,

90   respectively) protocols [45,49] recently allowed us to perform high-resolutions 3D immunofluorescence analyses

91   of thick RABV-infected tissues slices [69,48].

92   Here, we investigated the *in vivo* spread of a highly virulent field RABV clone (rRABV Dog) through the CNS

93   and PNS after intramuscular (i.m.) and intracranial (i.c.) inoculation. Using 3D immunofluorescence imaging of

94   solvent-cleared tissues by light sheet and confocal laser scanning microscopy, we identified RABV infections in

95   hind leg nerves, spinal cord, brain, and nerves of the facial region. These data provide a broad overview of field

96   RABV distribution in the clinical phase of rabies encephalitis. Notably, we were able to identify Schwann cells

97   (SCs) as a so far unrecognized non-neuronal RABV target cell population, which may be involved in regulating

98   RABV infection and, thus, pathogenesis in peripheral nerve tissues. Moreover, infection of SCs after centrifugal

99   RABV spread provides evidence for anterograde axonal transport and infectious virus release at distal axon

100   membrane sites of peripheral neurons.

101

102

4

Materials and Methods

103 **Viruses.** The recombinant field virus clone rRABV Dog [43] was derived from an isolate originating from an

105 infected dog from Azerbaijan, which was used in a challenge study [64]. RABV Bat (FLI virus archive ID N

106 13240) was isolated from an insectivorous North American bat.

107 **Animal trials.** Six- to eight-week-old BALB/c mice (Charles-River, Germany) were i.m.-infected with decreasing

108 doses of rRABV Dog. Four groups of six animals each were anesthetized with isoflurane and infected with $3x10^0$,

109 $3x10^1$, $3x10^2$ and $3x10^3$ $TCID_{50}$/mouse by injection of 30 µL of virus suspension in the femoral hind leg muscle.

110 Additionally, three mice were i.c.-infected at a dose of $1x10^2$ $TCID_{50}$/mouse. Body weight and clinical scores from

111 one to five (1: ruffled fur, hunched back; 2: slowed movement, circular motions, weight loss > 15%; 3: tremors,

112 shaky movement, seizures, weight loss > 20%; 4: paralysis, weight loss > 25%; 5: coma/death) were determined

113 daily until day 21 post-infection or day of euthanasia. After reaching a clinical score of two, the animals were

114 anaesthetized with isoflurane and euthanized by decapitation. Samples were taken, fixed with 4%

115 paraformaldehyde (PFA) for one week, and stored for further processing. All remaining animals were euthanized

116 at 21 dpi. The animal approaches were evaluated by the responsible animal care, use, and ethics committee of the

117 State Office for Agriculture, Food Safety, and Fishery in Mecklenburg-Western Pomerania (LALFF M-V) and

118 gained approval with permission 7221.3-2-047/19). For RABV Bat, archived tissue samples (hind legs, spinal

119 columns, and heads) from previous virus characterization experiments were used (LALFF M-V permission

120 7221.3-2.1-001/18).

121 **Detection of RABV RNA in oral swabs and salivary glands via RT-PCR.** Salivary gland samples were

122 homogenized in 1 ml cell culture medium in the UPHO Ultimate Homogenizer (Geneye, Hong Kong) using a 3

123 mm steal bead. Oral swab samples were transferred into 1 ml of culture medium. Total RNA from oropharyngeal

124 swabs as well as from salivary gland tissues were extracted using the NucleoMagVet kit (Macherey&Nagel,

125 Germany) according to manufacturer's instructions in a KingFisher/BioSprint 96 magnetic particle processor

126 (Qiagen, Germany). RABV RNA was detected by the R14-assay, a RT-qPCR targeting the N-gene [27]. The RT-

127 qPCR reaction was prepared using the AgPath-ID-One-Step RT-PCR kit (Thermo Fisher Scientific, USA) adjusted

128 to a volume of 12.5 µl [19]. RT-qPCRs were performed on a BioRad real-time CFX96 detection system (Bio-Rad,

129 USA).

130 **Antibodies and dyes.** To detect RABV in the tissues, a polyclonal rabbit serum against recombinant RABV P

131 protein (P160-5; 1:3,000 in PTwH [0.2% Tween 20 in PBS with 10 µg/mL heparin]) was used [44]. The following

132 first antibodies and dyes were obtained from the respective suppliers: chicken anti-NEFM (Thermo Fisher, USA;

133 #PA1-16758, RRID:AB_2282551; 1:1,000 in PTwH), guinea pig anti-NEFM (Synaptic Systems, Germany;

134 #171204, RRID:AB_2619872; 1:400 in PTwH), chicken anti-MBP (Thermo Fisher; #PA1-10008,

135 RRID:AB_1077024; 1:500 in PTwH), TO-PRO$^{\text{TM}}$-3 iodide (Thermo Fisher; #T3605; 1:1,000 in PTwH.) As

136 secondary antibodies donkey anti-rabbit Alexa Fluor® 568 (Thermo Fisher; #A10042, RRID:AB_2534017),

137 donkey anti-chicken Alexa Fluor® 488 (Dianova, Germany; #703-545-155, RRID:AB_2340375), donkey anti-

138 guinea pig Alexa Fluor® 647 (Dianova; #706-605-148, RRID:AB_10895029) were used, each at dilution of 1:500

139 in PTwH.

140 **iDISCO-based immunostaining and uDISCO-based clearing of tissue samples.** Staining and clearing

141 protocols were adapted from earlier reports [45,49] and were performed as described previously [69,48]. Hind legs

142 were skinned prior to fixation. Prior to the slicing, PFA-fixed hard tissues, which included hind legs, spinal

143 columns, and heads, were decalcified with 20% ethylenediaminetetraacetic acid (EDTA) [w/v] in H_2O_{dd} (pH was

144 adjusted to 7.0) for four days at 37 °C. The EDTA solution was exchanged daily. Afterwards the decalcified tissues

145 were cut into 1 mm thick sections using a scalpel. For brains, as soft tissues, a vibratome (VT1200S, Leica

146 Biosystems, Germany) was used. After treatment with increasing methanol concentrations in distilled water (20%,

147 40%, 60%, 80%, and twice 100%) and bleaching with 5% H_2O_2 in pure methanol at 4 °C, the samples were

148 rehydrated with decreasing concentrations of methanol in distilled water (80%, 60%, 40%, and 20%). After

149 washing with PBS and 0.2% Triton X-100 in PBS, the samples were permeabilized for 2 days at

150 37 °C in 0.2% Triton X-100/20% DMSO/0.3 M glycine in PBS. After subsequent blocking with 6% donkey

151 serum/0.2% Triton X-100/10% DMSO in PBS at 37 °C for another 48 h, primary antibodies in PTwH were added

152 for 5 days with refreshment of the antibody solution after 2.5 days. The samples were washed with PTwH four

153 times until the next day, when secondary antibodies in PTwH were added for 5 days with refreshment of the

154 antibody solution after 2.5 days. After further washing for four times until the next day, the tissues were dehydrated

155 by a series of *tert*-butanol (TBA) solutions (from 30% to 96% in distilled water), each step for 2 h (except over

156 night incubation with for 80% TBA), final incubation in 100% TBA and subsequent clearing in BABB-D15 with

157 0.4 vol% DL-α-tocopherol until they were optically transparent (2 – 6 h). BABB-D15 is a combination of benzyl

158 alcohol (BA) and benzyl benzoate (BB) at a ratio of 1:2, which is mixed at a ratio of 15:1 with diphenyl ether

159 (DPE). The samples were either analyzed directly by light sheet microscopy or were transferred to 3D-printed

160 imaging chambers as described before (Zaeck et al., 2019.)

161 **Light sheet and confocal laser scanning microscopy.** For light sheet microscopy, a LaVision UltraMicroscope

162 II with an Andor Zyla 5.5 sCMOS Camera, an Olympus MVX-10 Zoom Body (magnification range: 0.63 – 6.3x),

163 and an Olympus MVPLAPO 2x objective (NA = 0.5) equipped with a dipping cap was used. Z-stacks were

164   acquired with a light sheet NA of 0.156, a light sheet width of 100%, and a z-step size of 2 µm. LaVision BioTec

165   ImSpector Software (v7.0.127.0) was used for image acquisition.

166   Confocal laser scanning microscopy was performed with a Leica DMI 6000 TCS SP5 equipped with a HC PL

167   APO CS2 40x water immersion objective (NA = 1.1; Leica, Germany; #15506360), using the Leica Application

168   Suite Advanced Fluorescence software (V. 2.7.3.9723) and a z-step size of 0.5 µm.

169   **Image processing.** For image processing, a Dell Precision 7920 workstation was used (CPU: Intel Xeon Gold

170   5118, GPU: Nvidia Quadro P5000, RAM: 128 GB 2666 MHz DDR4, SSD: 2 TB). Acquired image stacks were

171   processed using the ImageJ (v1.52h) distribution package Fiji [53,54] or arivis Vision4D (arivis, Germany; v3.2.0).

172   Brightness and contrast were adjusted for each channel and, if necessary, channels were denoised. Either

173   maximum-z-projections or volumetric 3D-projections are shown.

174

7

175 **Results**

176 **Field virus clone rRABV Dog undergoes the complete RABV infection cycle in adult BALC/c mice.** Mouse

177 models differ in their age-dependent susceptibility to fixed RABV lab strains and field isolates [11]. To confirm

178 the field virus character of rRABV Dog and its suitability for investigation of the complete RABV *in vivo* cycle

179 from infected muscle at the site of entry to secretion in saliva in adult mice, six- to eight-week-old BALB/c mice

180 were inoculated by the i.m. route (hind leg muscle) with decreasing infectious virus doses. Although mortality was

181 dose-dependent, even very low doses (30 $TCID_{50}$/mouse) of rRABV Dog were sufficient to cause rabies disease

182 and release of infectious virus in nearly all inoculated mice, thus, highlighting the high virulence of this field virus

183 RABV clone. Comparable to field RABV isolates, even at an extremely low infection dose (3 $TCID_{50}$/mouse), the

184 complete *in vivo* cycle had been undergone by animals that succumbed to infection, as shown by detection of viral

185 RNA in both salivary glands and in oral swabs using RT-qPCR (Table 1; Fig. S1).

186 **Table 1: Dose-dependent onset of clinical rabies signs after i.m. application of rRABV Dog in the upper**

187 **hind leg muscle of six- to eight-week old BALB/c mice.** Salivary gland and oral swabs were virus RNA positive

188 even at low infection doses. *One oral swab not tested.

virus dose	euthanized	salivary gland	oral swab
TCID50/mouse	(humane endpoint reached)	virus RNA	virus RNA
3,000	6/6	6/6	5*/6
300	5/6	5/6	5/6
30	5/6	5/6	5/6
3	2/6	2/6	2/6

189

190 **RABV infects peripheral neuron-associated neuroglia in the hind leg after i.m. inoculation.** Immunostaining

191 of solvent-cleared hind leg slices of diseased animals for RABV phosphoprotein (P), neurofilament M (NEFM),

192 and cell nuclei (TO-PRO™-3) was performed for light sheet and confocal laser scanning microscopy analysis (Fig.

193 1). RABV infection of peripheral nerves innervating the femoral tissue could be demonstrated (Fig. 1 A-C, red).

194 Reconstruction of a 3D femoral tissue volume allowed visualization of the distribution of infected nerve fibres in

195 their spatial environment (Fig. 1B, Video S1). The specificity of the RABV immunofluorescence was confirmed

196 by using non-infected hind leg tissues as negative controls (Fig. S3). At a higher resolution, axons were identified

197 via staining by the neuronal cytoskeleton marker (NEFM) (Fig. 1D,E, green) but, notably, did not co-localize with

198 RABV P (Fig. 1E). As RABV-infected peripheral nerves could be visualized in all serial femoral slices analysed

8

199   (Fig. 1F-J), our approach proved to be appropriate to reconstruct a 3D model of RABV infection patterns in

200   peripheral tissues.

201   Further confocal laser scanning analysis confirmed the lack of co-localization of RABV P with NEFM in axons

202   (Fig. 2A,B). Rather, RABV P specific signals were arranged next to or around the tubular NEFM signals (Fig.

203   2C,D, arrows; Video S2). Similar spatial arrangement patterns were observed after staining for the Schwann cell

204   (SC) marker myelin basic protein (MBP) (Fig. 2E-K). MBP is known to be part of the myelin sheath of SCs that

205   forms tubular structures around the axons (reviewed in [51]) and accordingly, appeared as hollow tubules that

206   were surrounded by RABV P (Fig. 2 G-K, arrowheads; Video S3). Corroborated by the presence of nuclei in

207   RABV-infected cells (Fig. 2K), this suggests that RABV P accumulated in the cytoplasm of axon-ensheathing

208   SCs. This provides evidence for the infection of and virus gene expression in neuroglia of the PNS in the clinical

209   phase of RABV encephalitis after i.m. infection.

210   **Infection of Schwann cells after i.c. inoculation strongly supports anterograde spread of RABV into the**

211   **periphery.** Late phase infection of myelinating SCs in the PNS of i.m.-infected mice could be a result of unspecific

212   virus release from abundantly and long-term RABV-infected myelinated neurons. To investigate, whether RABV

213   also enters the PNS after centrifugal spread from the brain and whether this also leads to infection of myelinating

214   SCs, femoral tissue from i.c.-infected mice was analyzed.

215   Detection of RABV antigen in the PNS revealed that innervating nerves in femoral tissue can get infected after

216   centrifugal spread of the virus from the brain (Fig. 3A-G). As observed for i.m. inoculations, RABV P fluorescence

217   signals surrounded rather than overlapped with NEFM-positive axons (Fig. 3D,E). Staining for RABV P, MBP,

218   and NEFM (Fig. 3F-K) revealed a three-layered structure with RABV P-specific signals surrounding the MBP-

219   sheath of axons (Fig. 3H-K, Video S4). Infection of myelinated SCs after i.c. inoculation demonstrated that

220   infectious virus was released from peripheral axons, infecting the surrounding axon-associated, non-neuronal cells.

221   **RABV exhibits a strong, infection route-independent infection of the spinal cord.** To assess the degree of

222   infection of the spinal cord by field virus clone rRABV Dog after different routes of infection, spinal column slices

223   (Fig. S2C) of i.m.- and i.c.-infected mice were systematically analyzed. Independent of the inoculation route,

224   multiple neurons in the spinal cord and neurons projecting out of the same were positive for RABV P (Fig. 4).

225   Higher magnification image stacks of the spinal cord revealed RABV P staining to be primarily localized in the

226   grey matter, surrounded by NEFM-positive white matter (Fig. 4C,I, star and triangle, respectively). Indeed, white

227   and grey matter (Fig. 4D,J, star and triangle, respectively) revealed multiple NEFM-positive axons of which some

228   were infected (Fig. 4E,K). In contrast to the peripheral femoral axons, where the RABV P staining almost

229   exclusively surrounded the tubular NEFM structures (Fig. 2C,D and 3D,E), here, RABV P- and NEFM-specific

230   signals perfectly co-localized (Fig. E,K), suggesting that the axons contained high levels of RABV P protein.

231   Peripheral nerves projecting from the spinal cord also revealed double positive axons (Fig. 4F-H, L-N). However,

232   also RABV P not overlapping with NEFM was observed (Fig. 4H, arrow). In some projecting axon bundles (Fig.

233   4L), almost all axons were RABV-positive as indicated by co-localization of RABV P and NEFM (Fig. 4M,N).

234   **Pronounced infection of various tissues and sensory neurons of the facial head region.** Since centrifugal

235   spread to the salivary glands is considered an inevitable step in RABV transmission to other hosts, the extent of

236   RABV infection in tissues of the facial head regions was investigated by imaging of coronal head slices (Fig. S2B).

237   Except for the olfactory bulb, the brain was removed prior to sectioning for separate processing. 3D volume

238   reconstruction from light sheet microscopy z-stacks demonstrated abundant RABV P specific signals throughout

239   various areas of the coronal head slice both after i.c. (Fig. 5A,B; Video S5) and i.m. inoculation (Fig. 6A,B, Fig.

240   S4; Video S6). RABV-infected cells could be identified in the orbital (Fig. 5C,D and 6C,D), nasal (Fig. 5E,F and

241   6E,F), and oral cavity (Fig. 5G-J and 6G-J). Morphologies of the infected cells revealed a structure typical for

242   sensory neurons in the olfactory epithelium and retina (Fig. 5D,F; Fig. S4) and indicated selective infection of

243   neuronal cells in these tissues. Notably, even though abundant route-independent infection of the olfactory bulb

244   was detectable, presence of fewer RABV-infected cells after i.m. inoculation as compared to the i.c. route

245   demonstrated inoculation route-dependent kinetics of the centrifugal spread to peripheral nerves (Fig. 5A and 6A).

246   Similar to the infection of femoral tissues (Fig. 2 and 3), RABV P was arranged around NEFM-positive axons

247   (Fig.5J, Fig 7A-E), indicating involvement of SCs. Accordingly, RABV was detected at the convex side of the

248   myelin sheaths (Fig. 7G-J, arrowheads; Video S7). This confirmed infection of neuroglia in RABV infection of

249   peripheral nerves of the facial head region. However, in single cases RABV P was also present inside the myelin

250   sheaths, indicating RABV P accumulation in the respective axons (Fig. 7I,J, stars).

251

252

10

Discussion

254   Using organic solvent-based organ clearing [45,49] for the 3D deep tissue imaging of RABV infections [69], we

255   aimed at investigating and systematically analyzing the *in vivo* cycle and main checkpoints of a highly virulent

256   field RABV (rRABV Dog) on its journey through the host's body. To this end, we provide an unprecedented

257   comprehensive overview of the local field RABV tissue tropism and spread in the late clinical phase of RABV

258   encephalitis based on high-volume immunofluorescence imaging. By analyzing peripheral tissues after both i.m.

259   and i.c. infection, we were not only able to visualize RABV infection in PNS and CNS neurons after centripetal

260   and centrifugal spread but also provide clear evidence for the infection of non-neuronal myelinating SCs in

261   peripheral nerves of hind legs and facial head regions (Fig. 2, 3 and 7). SCs constitute a glial cell type in the PNS

262   that functionally correlates to myelinating oligodendrocytes in the CNS (reviewed in [20]). Another important

263   finding is the corroboration of anterograde transport and spread of RABV in axons of peripheral nerves by infection

264   of the SCs after centrifugal spread from the CNS.

265   Myelinating SCs are peripheral neuroglia, which form the myelin sheath around axons of motor and sensory

266   neurons and, like oligodendrocytes in the CNS, are involved in saltatory conduction and trophic support for

267   neurons (reviewed in [51]). In peripheral nerves, RABV infection was associated with axon demyelination

268   [37,38,57,14,55]. T-lymphocyte-dependent immune pathogenesis was identified to be causative for RABV-

269   mediated neurotic paralysis, the disintegration of myelin sheaths, and the degeneration of axons [65]. Furthermore,

270   there has been speculation that involvement of rabies-induced neuropathogenesis in peripheral nerves results in

271   the typical rabies sings of muscle spasms and deglutition [37].

272   Although there are indications that SCs are somehow affected by RABV infections [14,37,38,55,57], evidence for

273   direct RABV infection of SCs in the PNS is lacking. While released RABV particles were detected at nodes of

274   Ranvier (known as myelin-sheath gaps occurring along a myelinated axon [40]) and between axonal and SC

275   plasma membranes [31,41,42]) only once infection of SCs is described [4]. Others failed to detect RABV infected

276   SCs (reviewed in [50]). Possible explanations for that may be the use of ultrathin sections in electron microscopy

277   in previous studies that run the inherent risk of missing rare events, RABV strain-specific differences in

278   accumulation in peripheral axons and SCs, and variations in the clinical phase of the analyzed animals.

279   SCs are immunocompetent and exert key functions in immune regulation by antigen presentation, pathogen

280   detection, and cytokine production [24,68]. Accordingly, productive or non-productive infection of these cells

281   could be critically important to immediate innate responses, local inflammatory processes, and the development

282   of adaptive immunity. Recently, we demonstrated that field RABVs, including the recombinant clone rRABV Dog

283   used in this study, are able to infect astroglia in the CNS to a remarkable degree comparable to neuron infections.

11

284   Whereas infection of astrocytes seems to be a hallmark of field RABVs, more attenuated lab strains are

285   characterized by highly restricted or absent infection of astrocytes. Accordingly, establishment of astroglia

286   infection by field RABVs was hypothesized to limit or block respective immune responses, subsequent virus

287   elimination, and delay immune pathology [48]. RABV infection of SCs in the PNS, as demonstrated in our study

288   (Figs. 2, 3 and 7), seems to represent a direct correlate to astroglia infection in the CNS. Comparable to the latter,

289   field RABV replication in peripheral neuroglia may result in local suppression of glia-mediated innate immune

290   responses and, thus, gain ability to replicate in SCs. In contrast, similar to the astroglia infection in the brain

291   [46,48], less virulent RABVs may infect SCs in an abortive manner because of a strong type I interferon response.

292   Evasion of innate and intrinsic antiviral pathways have been attributed to the RABV nucleoprotein (N), P, and

293   matrix (M) proteins [10,9,8,36,62]. As discussed above, there is reason to believe that, similar to current

294   hypotheses about the role of neuroglia infection in the CNS, virus variants are not or only inefficiently able to

295   establish infection in peripheral neuroglia. This may induce stronger local interferon responses, more severe local

296   immune pathogenesis, reduced virus replication, and damage of infected neurons. While we could even confirm

297   infection of SCs by another, bat-associated field RABV (Fig. S5), analyses with less virulent lab-adapted strains

298   and live-attenuated vaccine viruses have to be subject of further studies to assess whether the virulence-dependent

299   difference in glial cell infection observed in the brain [48] can be transferred to the SC infections in the PNS

300   described in this study.

301   Virus infection of peripheral SCs in hind legs and facial head regions by centrifugal spread after i.c. inoculation

302   (Figs. 3 and 7) as well as infection of sensory neurons in the olfactory epithelium and other tissues (Figs. 5 and 6)

303   provide evidence for anterograde transport of RABV along axons *in vivo*, something that has been attributed to

304   late phases of infection [16]. The long distance from the neuron soma in the respective ganglia and the tight spatial

305   association of the infected neuroglia with the axons makes it exceedingly unlikely that virus release at cell bodies

306   and extra-neuronal spread is responsible for distal SC infections.

307   Both *in vitro* and *in vivo* virus tracking already demonstrated that anterograde RABV transport through axons of

308   peripheral DRG neurons and other peripheral neurons is possible [3,60,6]. However, anterograde virus spread was

309   discussed to occur only in a passive, kinesin-independent manner and the release of infectious virus was called

310   into question [61]. Fast, post-replicative, and glycoprotein (G)-dependent anterograde axonal transport of RABV

311   in cultured DRG neurons, however, provided evidence for active transport to distal axon sites [6]. One reason for

312   the discrepancy observed between *in vitro* tracking and *in vivo* trans-neuronal tracing approaches could be the role

313   of peripheral neuroglia as major innate immune mediators in infected nerves as discussed earlier. Since the

314   standard neuronal tracer virus CVS-11 is less effective in infecting astrocytes in the brain [48], a strong local

12

315   antiviral immune response at peripheral sites may hinder CVS-11 replication in neuroglia target cells. Moreover,

316   anterogradely transported virus particles in axons may remain below the limit of detection in conventional *in vivo*

317   tracing approaches. Accordingly, anterograde transport in CVS-11 infection may have been overlooked because

318   peripheral neuroglia, which were used here as an indicator for anterograde spread of the used field RABV, might

319   not or only get abortively infected.

320   Beyond RABV spread in peripheral hind leg nerves after i.m. and i.c. infection, a more generalized roadmap of

321   RABV infection in the CNS and PNS could be build. As for human [58,32] and numerous animal samples (e.g.

322   [34,29,28]), abundant RABV specific signals in the spinal cord and brain could be observed (Fig. 4 and Fig. S6).

323   Virus detection in the orbital, nasal, and oral cavity confirmed previous reports about presence of RABV and

324   related lyssaviruses in a variety of other tissues [17,30,22,1], including retinal ganglion cells, their axons, and

325   lacrimal glands [25,15]. Considering the latter, a potential role of lacrimal glands in virus secretion has been

326   discussed [15]. Whereas lacrimal fluid may not contribute to the transmission of infectious virus to new hosts via

327   saliva, multiple infected sensory neurons in the olfactory and tongue epithelia (Fig. 5 and 6) with a direct

328   connection to the nasopharynx raise the question whether virus secretion at these sites could contribute to the total

329   amount of infectious virus in the salvia. For bat lyssaviruses, for instance, viral antigen was also detected in taste

330   buds of experimentally [22] and naturally infected animals [52].

331   **Conclusions**

332   By providing a comprehensive and detailed overview of RABV distribution in peripheral tissues after natural (i.m.)

333   and artificial (i.c.) routes of inoculation, we highlight novel insights in the cell tropism and *in vivo* spread of field

334   RABV. Importantly, by unveiling the infection of peripheral neuroglia, we suggest a model in which field RABV

335   infection of immunocompetent SCs is critically important for local innate immune responses in peripheral nerves.

336   This may not only contribute to the delayed immune detection of field RABVs through RABV mediated innate

337   immune response suppression in field virus infected SCs, but may also may explain the high neuroinvasive

338   potential of field RABVs when compared with less virulent lab virus strains, and manifestation of clinical

339   symptoms observed in infected animals and humans. Moreover, by demonstrating infection of myelinating SCs

340   after centrifugal spread from infected brains, we provide evidence for anterograde spread of infectious RABV

341   through axons of the peripheral nerve systems in clinical phases of rabies encephalitis.

342

343

344   **Abbrevitations**

345   BA: benzyl alcohol

346   BB: benzyl benzoate

347   CNS: central nervous system

348   DPE: diphenyl ether.

349   DRG: dorsal root ganglion

350   EDTA: ethylenediaminetetraacetic acid

351   G: glycoprotein

352   i.m.: intramuscular

353   i.c .: intracranial

354   LALFF M-V: State Office for Agriculture, Food Safety, and Fishery in Mecklenburg-Western Pomerania

355   M: matrix protein

356   MBP: marker myelin basic protein

357   N: nucleoprotein

358   NEFM: neurofilamten M

359   P: phosphoprotein

360   PNS: peripheral nervous system

361   RABV: rabies virus

362   PFA: paraformaldehyde

363   RNPs: ribonucleoproteins

364   SC: Schwann cell

365   TBA: *tert*-butanol

366   **Declarations**

367   **Ethics Approval**

368   No human material was used in this study. Animal trials have been evaluated by the ethics committee of the State

369   Office for Agriculture, Food Safety, and Fishery in Mecklenburg-Western Pomerania (LALFF M-V) and gained

370   approval with permission 7221.3-2-047/19 and 7221.3-2.1-001/18.

371

372   **Acknowledgements**

373   We thank Angela Hillner and Katrin Giesow for technical assistance.

374

References

1. Allendorf SD, Cortez A, Heinemann MB, Harary CM, Antunes JM, Peres MG et al (2012) Rabies virus distribution in tissues and molecular characterization of strains from naturally infected non-hematophagous bats. Virus research 165:119-125. doi:10.1016/j.virusres.2012.01.011

2. Amarasinghe GK, Arechiga Ceballos NG, Banyard AC, Basler CF, Bavari S, Bennett AJ et al (2018) Taxonomy of the order Mononegavirales: update 2018. Archives of virology 163:2283-2294. doi:10.1007/s00705-018-3814-x

3. Astic L, Saucier D, Coulon P, Lafay F, Flamand A (1993) The CVS strain of rabies virus as transneuronal tracer in the olfactory system of mice. Brain Res 619:146-156. doi:10.1016/0006-8993(93)91606-s

4. Atanasiu P, Sisman J (1967) [Morphological aspects of rabies virus]. Bull Off Int Epizoot 67:521-533

5. Balachandran A, Charlton K (1994) Experimental rabies infection of non-nervous tissues in skunks (Mephitis mephitis) and foxes (Vulpes vulpes). Vet Pathol 31:93-102. doi:10.1177/030098589403100112

6. Bauer A, Nolden T, Schroter J, Romer-Oberdorfer A, Gluska S, Perlson E et al (2014) Anterograde glycoprotein-dependent transport of newly generated rabies virus in dorsal root ganglion neurons. Journal of virology 88:14172-14183. doi:10.1128/JVI.02254-14

7. Begeman L, GeurtsvanKessel C, Finke S, Freuling CM, Koopmans M, Muller T et al (2018) Comparative pathogenesis of rabies in bats and carnivores, and implications for spillover to humans. Lancet Infect Dis 18:e147-e159. doi:10.1016/S1473-3099(17)30574-1

8. Besson B, Sonthonnax F, Duchateau M, Ben Khalifa Y, Larrous F, Eun H et al (2017) Regulation of NF-kappaB by the p105-ABIN2-TPL2 complex and RelAp43 during rabies virus infection. PLoS Pathog 13:e1006697. doi:10.1371/journal.ppat.1006697

9. Brzozka K, Finke S, Conzelmann KK (2005) Identification of the rabies virus alpha/beta interferon antagonist: phosphoprotein P interferes with phosphorylation of interferon regulatory factor 3. Journal of virology 79:7673-7681. doi:10.1128/JVI.79.12.7673-7681.2005

10. Brzozka K, Finke S, Conzelmann KK (2006) Inhibition of interferon signaling by rabies virus phosphoprotein P: activation-dependent binding of STAT1 and STAT2. Journal of virology 80:2675-2683. doi:10.1128/JVI.80.6.2675-2683.2006

11. Casals J (1940) Influence of Age Factors on Susceptibility of Mice to Rabies Virus. J Exp Med 72:445-451. doi:10.1084/jem.72.4.445

12. Charlton KM, Casey GA (1979) Experimental rabies in skunks: immunofluorescence light and electron microscopic studies. Lab Invest 41:36-44

406   13. Charlton KM, Nadin-Davis S, Casey GA, Wandeler AI (1997) The long incubation period in rabies: delayed

407   progression of infection in muscle at the site of exposure. Acta Neuropathol 94:73-77.

408   doi:10.1007/s004010050674

409   14. Chopra JS, Banerjee AK, Murthy JM, Pal SR (1980) Paralytic rabies: a clinico-pathological study. Brain

410   103:789-802. doi:10.1093/brain/103.4.789

411   15. Dalton MF, Siepker CL, Maboni G, Sanchez S, Rissi DR (2020) Ocular and Lacrimal Gland Lesions in

412   Naturally Occurring Rabies of Domestic and Wild Mammals. Vet Pathol 57:409-417.

413   doi:10.1177/0300985820911458

414   16. Davis BM, Rall GF, Schnell MJ (2015) Everything You Always Wanted to Know About Rabies Virus (But

415   Were Afraid to Ask). Annu Rev Virol 2:451-471. doi:10.1146/annurev-virology-100114-055157

416   17. Fekadu M, Shaddock JH (1984) Peripheral distribution of virus in dogs inoculated with two strains of rabies

417   virus. Am J Vet Res 45:724-729

418   18. Finke S, Conzelmann KK (2005) Replication strategies of rabies virus. Virus research 111:120-131.

419   doi:10.1016/j.virusres.2005.04.004

420   19. Fischer M, Freuling CM, Muller T, Wegelt A, Kooi EA, Rasmussen TB et al (2014) Molecular double-check

421   strategy for the identification and characterization of European Lyssaviruses. Journal of virological

422   methods 203:23-32. doi:10.1016/j.jviromet.2014.03.014

423   20. Fontenas L, Kucenas S (2017) Livin' On The Edge: glia shape nervous system transition zones. Curr Opin

424   Neurobiol 47:44-51. doi:10.1016/j.conb.2017.09.008

425   21. Fooks AR, Cliquet F, Finke S, Freuling C, Hemachudha T, Mani RS et al (2017) Rabies. Nat Rev Dis

426   Primers 3:17091. doi:10.1038/nrdp.2017.91

427   22. Freuling C, Vos A, Johnson N, Kaipf I, Denzinger A, Neubert L et al. (2009) Experimental infection of

428   serotine bats (Eptesicus serotinus) with European bat lyssavirus type 1a. The Journal of general

429   virology 90:2493-2502. doi:10.1099/vir.0.011510-0

430   23. Gluska S, Zahavi EE, Chein M, Gradus T, Bauer A, Finke S et al (2014) Rabies Virus Hijacks and

431   accelerates the p75NTR retrograde axonal transport machinery. PLoS Pathog 10:e1004348.

432   doi:10.1371/journal.ppat.1004348

433   24. Gold R, Archelos JJ, Hartung HP (1999) Mechanisms of immune regulation in the peripheral nervous

434   system. Brain Pathol 9:343-360. doi:10.1111/j.1750-3639.1999.tb00231.x

435   25. Haltia M, Tarkkanen A, Kivela T (1989) Rabies: ocular pathology. Br J Ophthalmol 73:61-67.

436   doi:10.1136/bjo.73.1.61

437   26. Hampson K, Coudeville L, Lembo T, Sambo M, Kieffer A, Attlan M et al (2015) Estimating the global

438   burden of endemic canine rabies. PLoS Negl Trop Dis 9:e0003709. doi:10.1371/journal.pntd.0003709

439   27. Hoffmann B, Freuling CM, Wakeley PR, Rasmussen TB, Leech S, Fooks AR et al (2010) Improved safety

440   for molecular diagnosis of classical rabies viruses by use of a TaqMan real-time reverse transcription-

441   PCR "double check" strategy. J Clin Microbiol 48:3970-3978. doi:10.1128/JCM.00612-10

442   28. Ito FH, Vasconcellos SA, Erbolato EB, Macruz R, Cortes Jde A (1985) Rabies virus in different segments of

443   brain and spinal cord of naturally and experimentally infected dogs. Int J Zoonoses 12:98-104

444   29. Jackson AC, Reimer DL (1989) Pathogenesis of experimental rabies in mice: an immunohistochemical

445   study. Acta Neuropathol 78:159-165. doi:10.1007/BF00688204

446   30. Jackson AC, Ye H, Phelan CC, Ridaura-Sanz C, Zheng Q, Li Z, Wan X et al (1999) Extraneural organ

447   involvement in human rabies. Lab Invest 79:945-951

448   31. Jenson AB, Rabin ER, Bentinck DC, Melnick JL (1969) Rabiesvirus neuronitis. Journal of virology 3:265-

449   269

450   32. Juntrakul S, Ruangvejvorachai P, Shuangshoti S, Wacharapluesadee S, Hemachudha T (2005) Mechanisms

451   of escape phenomenon of spinal cord and brainstem in human rabies. BMC Infect Dis 5:104.

452   doi:10.1186/1471-2334-5-104

453   33. Klingen Y, Conzelmann KK, Finke S (2008) Double-labeled rabies virus: live tracking of enveloped virus

454   transport. Journal of virology 82:237-245. doi:10.1128/JVI.01342-07

455   34. Kojima D, Park CH, Satoh Y, Inoue S, Noguchi A, Oyamada T (2009) Pathology of the spinal cord of

456   C57BL/6J mice infected with rabies virus (CVS-11 strain). J Vet Med Sci 71:319-324.

457   doi:10.1292/jvms.71.319

458   35. Li J, McGettigan JP, Faber M, Schnell MJ, Dietzschold B (2008) Infection of monocytes or immature

459   dendritic cells (DCs) with an attenuated rabies virus results in DC maturation and a strong activation of

460   the NFkappaB signaling pathway. Vaccine 26:419-426. doi:10.1016/j.vaccine.2007.10.072

461   36. Masatani T, Ito N, Shimizu K, Ito Y, Nakagawa K, Sawaki Y et al (2010) Rabies virus nucleoprotein

462   functions to evade activation of the RIG-I-mediated antiviral response. Journal of virology 84:4002-

463   4012. doi:10.1128/JVI.02220-09

464   37. Minguetti G, Hofmeister RM, Hayashi Y, Montano JA (1997) Ultrastructure of cranial nerves of rats

465   inoculated with rabies virus. Arq Neuropsiquiatr 55:680-686. doi:10.1590/s0004-282x1997000500002

466   38. Minguetti G, Negrao MM, Hayashi Y, de Freitas OT (1979) Ultrastructure of peripheral nerves of mice

467   inoculated with rabies virus. Arq Neuropsiquiatr 37:105-112. doi:10.1590/s0004-282x1979000200001

468   39. Morimoto K, Hooper DC, Carbaugh H, Fu ZF, Koprowski H, Dietzschold B (1998) Rabies virus

469   quasispecies: implications for pathogenesis. Proceedings of the National Academy of Sciences of the

470   United States of America 95:3152-3156. doi:10.1073/pnas.95.6.3152

471   40. Murphy FA (1977) Rabies pathogenesis. Archives of virology 54:279-297. doi:10.1007/BF01314774

472   41. Murphy FA, Bauer SP, Harrison AK, Winn WC, Jr. (1973) Comparative pathogenesis of rabies and rabies-

473   like viruses. Viral infection and transit from inoculation site to the central nervous system. Lab Invest

474   28:361-376

475   42. Murphy FA, Harrison AK, Winn WC, Bauer SP (1973) Comparative pathogenesis of rabies and rabies-like

476   viruses: infection of the central nervous system and centrifugal spread of virus to peripheral tissues. Lab

477   Invest 29:1-16

478   43. Nolden T, Pfaff F, Nemitz S, Freuling CM, Hoper D, Muller T et al (2016) Reverse genetics in high

479   throughput: rapid generation of complete negative strand RNA virus cDNA clones and recombinant

480   viruses thereof. Sci Rep 6:23887. doi:10.1038/srep23887

481   44. Orbanz J, Finke S (2010) Generation of recombinant European bat lyssavirus type 1 and inter-genotypic

482   compatibility of lyssavirus genotype 1 and 5 antigenome promoters. Archives of virology 155:1631-

483   1641. doi:10.1007/s00705-010-0743-8

484   45. Pan C, Cai R, Quacquarelli FP, Ghasemigharagoz A, Lourbopoulos A, Matryba P, Plesnila N, Dichgans M,

485   Hellal F, Erturk A (2016) Shrinkage-mediated imaging of entire organs and organisms using uDISCO.

486   Nature methods 13:859-867. doi:10.1038/nmeth.3964

487   46. Pfefferkorn C, Kallfass C, Lienenklaus S, Spanier J, Kalinke U, Rieder M et al (2016) Abortively Infected

488   Astrocytes Appear To Represent the Main Source of Interferon Beta in the Virus-Infected Brain.

489   Journal of virology 90:2031-2038. doi:10.1128/JVI.02979-15

490   47. Piccinotti S, Whelan SP (2016) Rabies Internalizes into Primary Peripheral Neurons via Clathrin Coated Pits

491   and Requires Fusion at the Cell Body. PLoS Pathog 12:e1005753. doi:10.1371/journal.ppat.1005753

492   48. Potratz M, Zaeck L, Christen M, Te Kamp V, Klein A, Nolden T et al (2020) Astrocyte Infection during

493   Rabies Encephalitis Depends on the Virus Strain and Infection Route as Demonstrated by Novel

494   Quantitative 3D Analysis of Cell Tropism. Cells 9. doi:10.3390/cells9020412

495   49. Renier N, Wu Z, Simon DJ, Yang J, Ariel P, Tessier-Lavigne M (2014) iDISCO: a simple, rapid method to

496   immunolabel large tissue samples for volume imaging. Cell 159:896-910.

497   doi:10.1016/j.cell.2014.10.010

498   50. Rossiter JP, Jackson AC (2020) Pathology. In: Rabies scientific basis of the disease and its management. 4th

499   edn. Academic Press, pp 347-371

500   51. Salzer JL (2015) Schwann cell myelination. Cold Spring Harb Perspect Biol 7:a020529.

501   doi:10.1101/cshperspect.a020529

502   52. Schatz J, Teifke JP, Mettenleiter TC, Aue A, Stiefel D, Muller T et al (2014) Lyssavirus distribution in

503   naturally infected bats from Germany. Vet Microbiol 169:33-41. doi:10.1016/j.vetmic.2013.12.004

504   53. Schindelin J, Arganda-Carreras I, Frise E, Kaynig V, Longair M, Pietzsch T et al (2012) Fiji: an open-source

505   platform for biological-image analysis. Nature methods 9:676-682. doi:10.1038/nmeth.2019

506   54. Schneider CA, Rasband WS, Eliceiri KW (2012) NIH Image to ImageJ: 25 years of image analysis. Nature

507   methods 9:671-675

508   55. Tangchai P, Vejjajiva A (1971) Pathology of the peripheral nervous system in human rabies. A study of nine

509   autopsy cases. Brain 94:299-306. doi:10.1093/brain/94.2.299

510   56. Te Kamp V, Freuling CM, Vos A, Schuster P, Kaiser C, Ortmann S, Kretzschmar A et al (2020)

511   Responsiveness of various reservoir species to oral rabies vaccination correlates with differences in

512   vaccine uptake of mucosa associated lymphoid tissues. Sci Rep 10:2919. doi:10.1038/s41598-020-

513   59719-4

514   57. Teixeira F, Aranda FJ, Castillo S, Perez M, Del Peon L, Hernandez O (1986) Experimental rabies:

515   ultrastructural quantitative analysis of the changes in the sciatic nerve. Exp Mol Pathol 45:287-293.

516   doi:10.1016/0014-4800(86)90017-1

517   58. Tirawatnpong S, Hemachudha T, Manutsathit S, Shuangshoti S, Phanthumchinda K, Phanuphak P (1989)

518   Regional distribution of rabies viral antigen in central nervous system of human encephalitic and

519   paralytic rabies. J Neurol Sci 92:91-99. doi:10.1016/0022-510x(89)90178-0

520   59. Tsiang H (1979) Evidence for an intraaxonal transport of fixed and street rabies virus. J Neuropathol Exp

521   Neurol 38:286-299. doi:10.1097/00005072-197905000-00008

522   60. Tsiang H, Lycke E, Ceccaldi PE, Ermine A, Hirardot X (1989) The anterograde transport of rabies virus in

523   rat sensory dorsal root ganglia neurons. The Journal of general virology 70 (Pt 8):2075-2085.

524   doi:10.1099/0022-1317-70-8-2075

525   61. Ugolini G (2010) Advances in viral transneuronal tracing. J Neurosci Methods 194:2-20.

526   doi:10.1016/j.jneumeth.2009.12.001

527 62. Vidy A, Chelbi-Alix M, Blondel D (2005) Rabies virus P protein interacts with STAT1 and inhibits

528   interferon signal transduction pathways. Journal of virology 79:14411-14420.

529   doi:10.1128/JVI.79.22.14411-14420.2005

530 63. Vos A, Freuling CM, Hundt B, Kaiser C, Nemitz S, Neubert A et al (2017) Oral vaccination of wildlife

531   against rabies: Differences among host species in vaccine uptake efficiency. Vaccine 35:3938-3944.

532   doi:10.1016/j.vaccine.2017.06.022

533 64. Vos A, Nolden T, Habla C, Finke S, Freuling C, Teifke J et al (2013) Raccoons (Procyon lotor) in Germany

534   as potential reservoir species for Lyssaviruses. Eur J Wildl Res 59:637-643. doi:10.1007/s10344-013-

535   0714-y

536 65. Weiland F, Cox JH, Meyer S, Dahme E, Reddehase MJ (1992) Rabies virus neuritic paralysis:

537   immunopathogenesis of nonfatal paralytic rabies. Journal of virology 66:5096-5099

538 66. Wickersham IR, Finke S, Conzelmann KK, Callaway EM (2007) Retrograde neuronal tracing with a

539   deletion-mutant rabies virus. Nature methods 4:47-49. doi:10.1038/nmeth999

540 67. Wickersham IR, Lyon DC, Barnard RJ, Mori T, Finke S, Conzelmann KK et al (2007) Monosynaptic

541   restriction of transsynaptic tracing from single, genetically targeted neurons. Neuron 53:639-647.

542   doi:10.1016/j.neuron.2007.01.033

543 68. Ydens E, Lornet G, Smits V, Goethals S, Timmerman V, Janssens S (2013) The neuroinflammatory role of

544   Schwann cells in disease. Neurobiol Dis 55:95-103. doi:10.1016/j.nbd.2013.03.005

545 69. Zaeck L, Potratz M, Freuling CM, Muller T, Finke S (2019) High-Resolution 3D Imaging of Rabies Virus

546   Infection in Solvent-Cleared Brain Tissue. Jove-J Vis Exp. doi:ARTN e59402 10.3791/59402

547 70. Zampieri N, Jessell TM, Murray AJ (2014) Mapping sensory circuits by anterograde transsynaptic transfer of

548   recombinant rabies virus. Neuron 81:766-778. doi:10.1016/j.neuron.2013.12.033

549

550
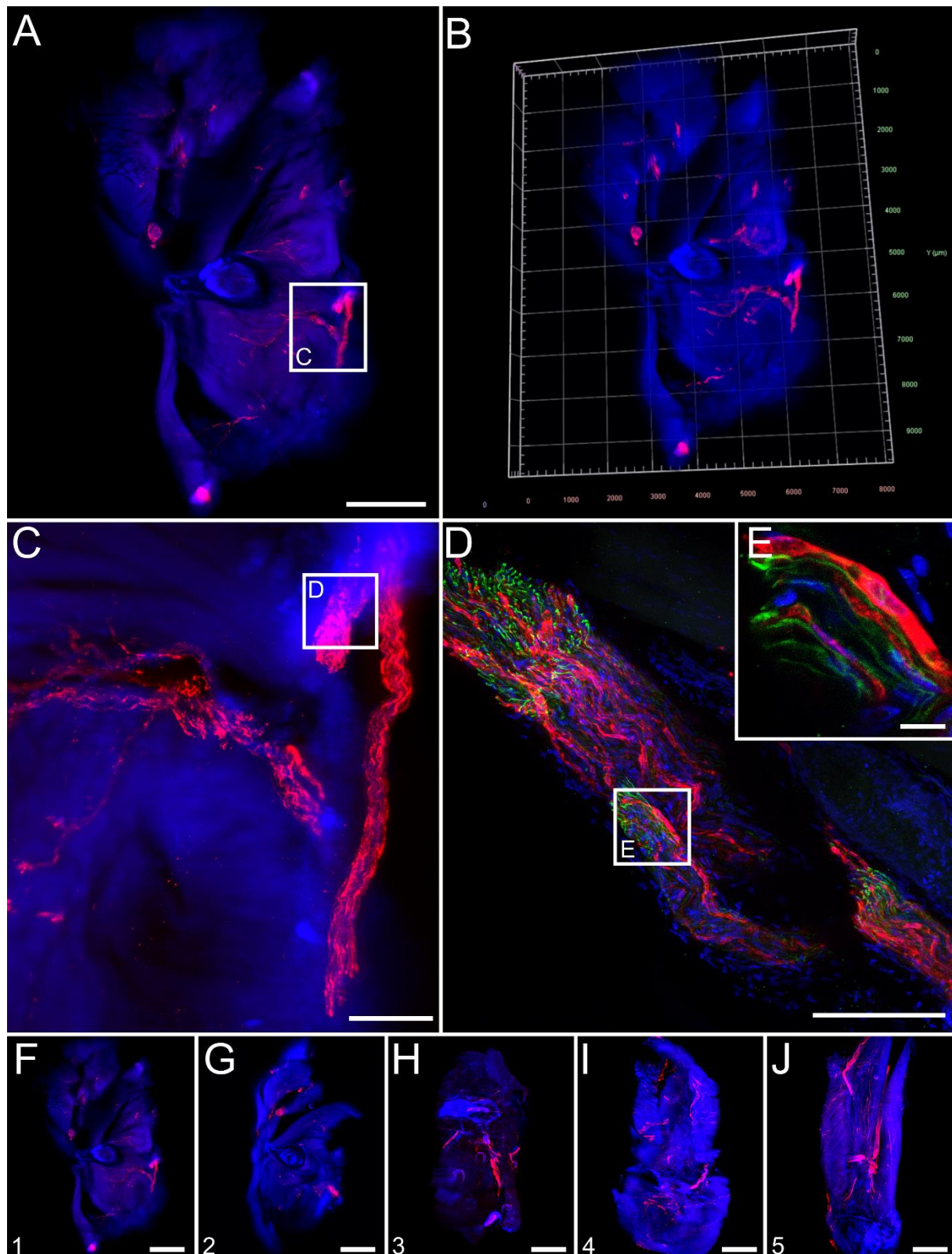
Fig. 1 Overview of field RABV infection in mouse hind leg cross sections after i.m. infection (9 days post-inoculation). **(A)** Maximum z-projection of light sheet overview of a hind leg cross section [1.6x magnification; z = 1,156 µm]. Red: RABV P; blue: nuclei. Green fluorescence for NEFM not shown as separation from green autofluorescence was not possible at low resolution. Scale bar: 1,500 µm. **(B)** 3D projection of (A). **(C)** Maximum z-projection of detail (white box in A) with infected nerve [12.6x magnification; z = 574 µm]. Scale bar: 200 µm.

21

557 **(D)** Maximum z-projection of confocal z-stack of indicated region in (C) [z = 48 µm] of infected nerve with NEFM

558 signal (green). Scale bar: 100 µm. Note: due to the separate image acquisition, the orientation of the shown nerve

559 is different to (C). **(E)** Maximum z-projection of detail from (D) [z = 10 µm]. Scale bar: 10 µm. **(F-J)** Maximum

560 z-projections of serial thick hind leg sections from the upper leg (F) to the knee (J) [1.6x magnification, z = 1,156

561 µm (F), 1,402 µm (G), 1,172 µm (H), 1,990 µm (I), 1,372 µm (J)]. For reference, see indicated slices in Fig. S2A.

562 For improved intelligibility, only RABV P (red) and nuclei (blue) are shown. Scale bar: 1,500 µm.

563

564
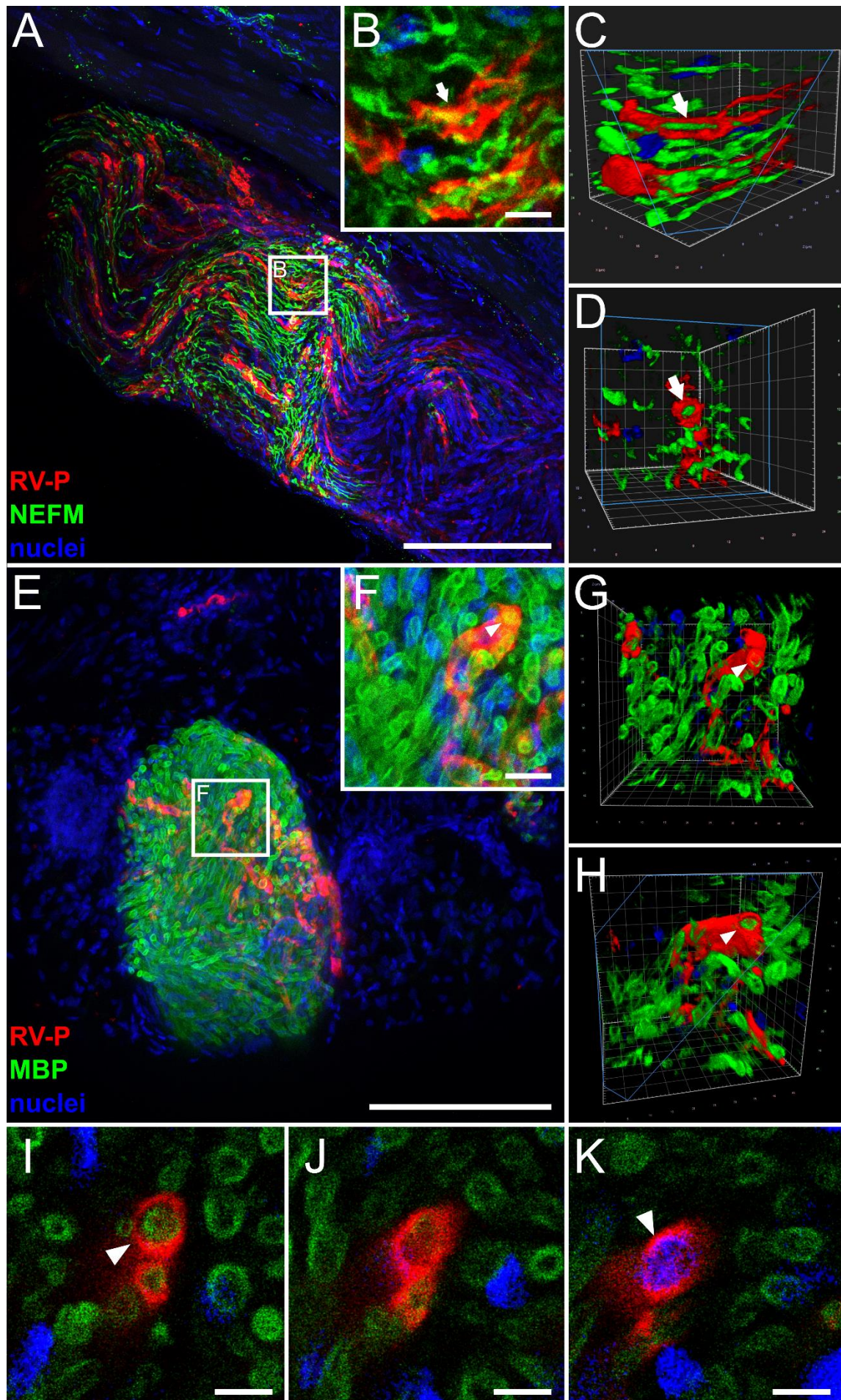
565   **Fig. 2** Detection of RABV P in non-neuronal Schwann cells of hind leg tissue after i.m. inoculation (9 days post-

566   inoculation). **(A,B)** Maximum z-projection of high-resolution confocal z-stacks of RABV-infected nerve fiber (see

567   also Fig. 1D) in hind leg sections [z = 45 µm; Scale bar: 100 µm] (A) and detail [z = 15 µm; Scale bar: 10 µm]

568   (B). Red: RABV P; green: NEFM; blue: cell nuclei. **(C,D)** Volumetric 3D projections of (B) with different viewing

569   angles. The light blue box indicates the clipping plane. Arrows: RABV P surrounding axonal NEFM. **(E,F)**

570   Maximum z-projection of a hind leg section (E) [z = 134 µm; Scale bar: 200 µm] and detail (F) [z = 20 µm; Scale

571   bar: 10 µm] stained for RABV P (red), MBP (green) and nuclei (blue). **(G,H)** Volumetric 3D projections of

572   different viewing angles of (F). Arrowhead: RABV-infected Schwann cell **(I-K)** Single slices with RABV P (red),

573   MBP (green) and nuclei (blue). Arrowheads indicate myelin sheath/nucleus surrounded by RABV P. Scale bar: 5

574   µm.

575

24

576
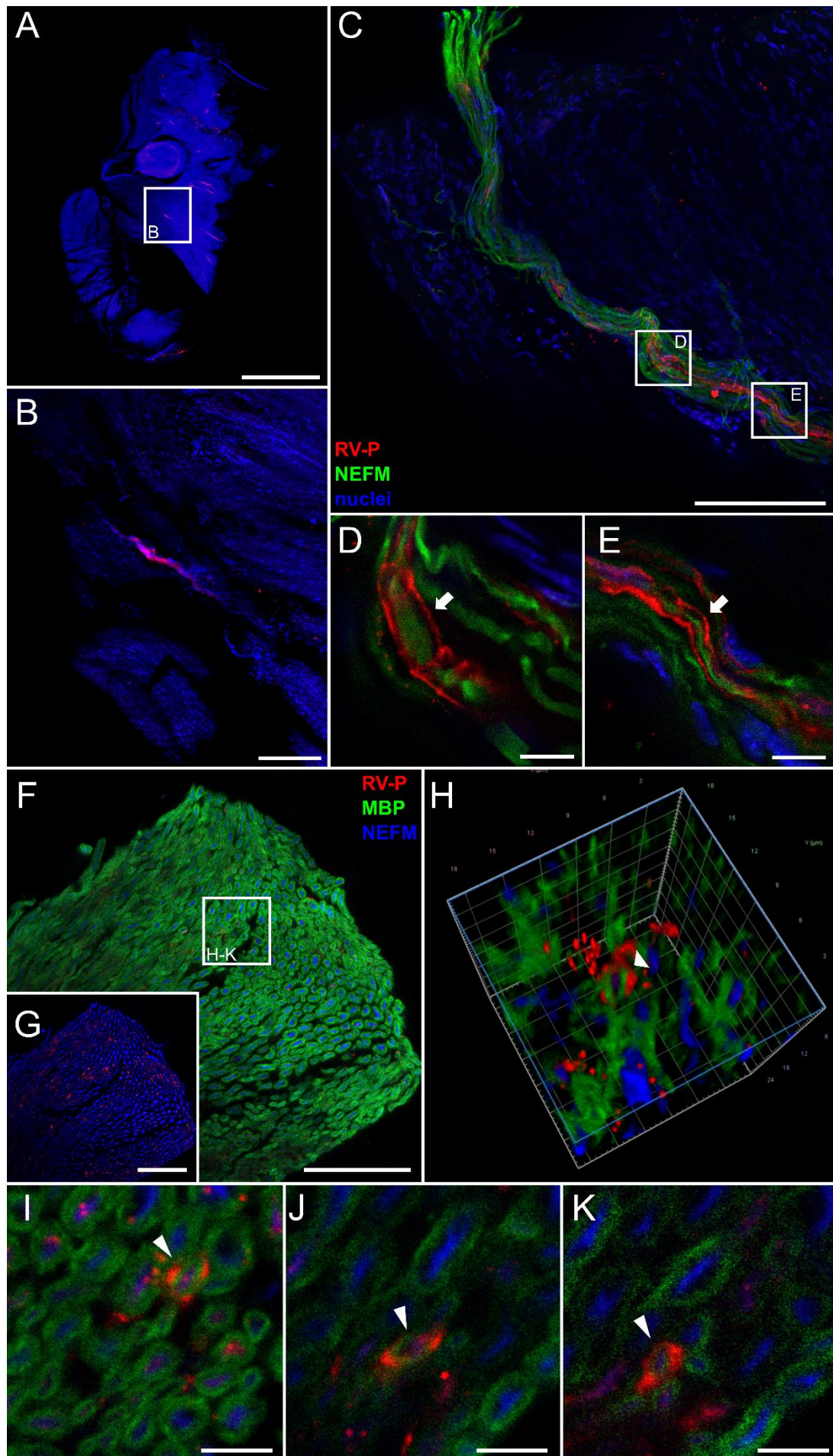
577 **Fig. 3 Anterograde virus spread: RABV in Schwann cells of a hind leg nerve after i.c. inoculation. (A,B)**

578 Maximum z-projection of light sheet overview (A) and detail (B) of hind leg section after staining for RABV P

579 (red), and nuclei (blue). Green fluorescence for NEFM is not shown as separation from green autofluorescence

580 was not possible at low resolution. (A) Magnification of 1.6x [z = 1,944 µm; Scale bar: 1,500 µm] and (B)

581 magnification of 12.6x [z = 58 µm; Scale bar: 200 µm]. **(C)** Maximum z-projection of confocal z-stack [z = 37

582 µm] of infected nerve fiber from (B), now including NEFM staining (green). Scale bar: 100 µm. **(D,E)** Maximum

583 z-projection of details from (C) (see white boxes) [z = 5 µm (D,E)]. Scale bar: 10 µm. **(F,G)** Maximum z-projection

584 of hind leg nerve section stained for RABV P (red), MBP (green) and NEFM (blue) [z = 15 µm]. To visualize low

585 amounts of viral antigen, the MBP channel is excluded in (G). Scale bar: 50 µm. **(H)** 3D projection of detail from

586 (F) (see white box). **(I-K)** Single planes from detail of (F). The arrowhead indicates an RABV-infected cell. Scale

587 bar: 5 µm.

588
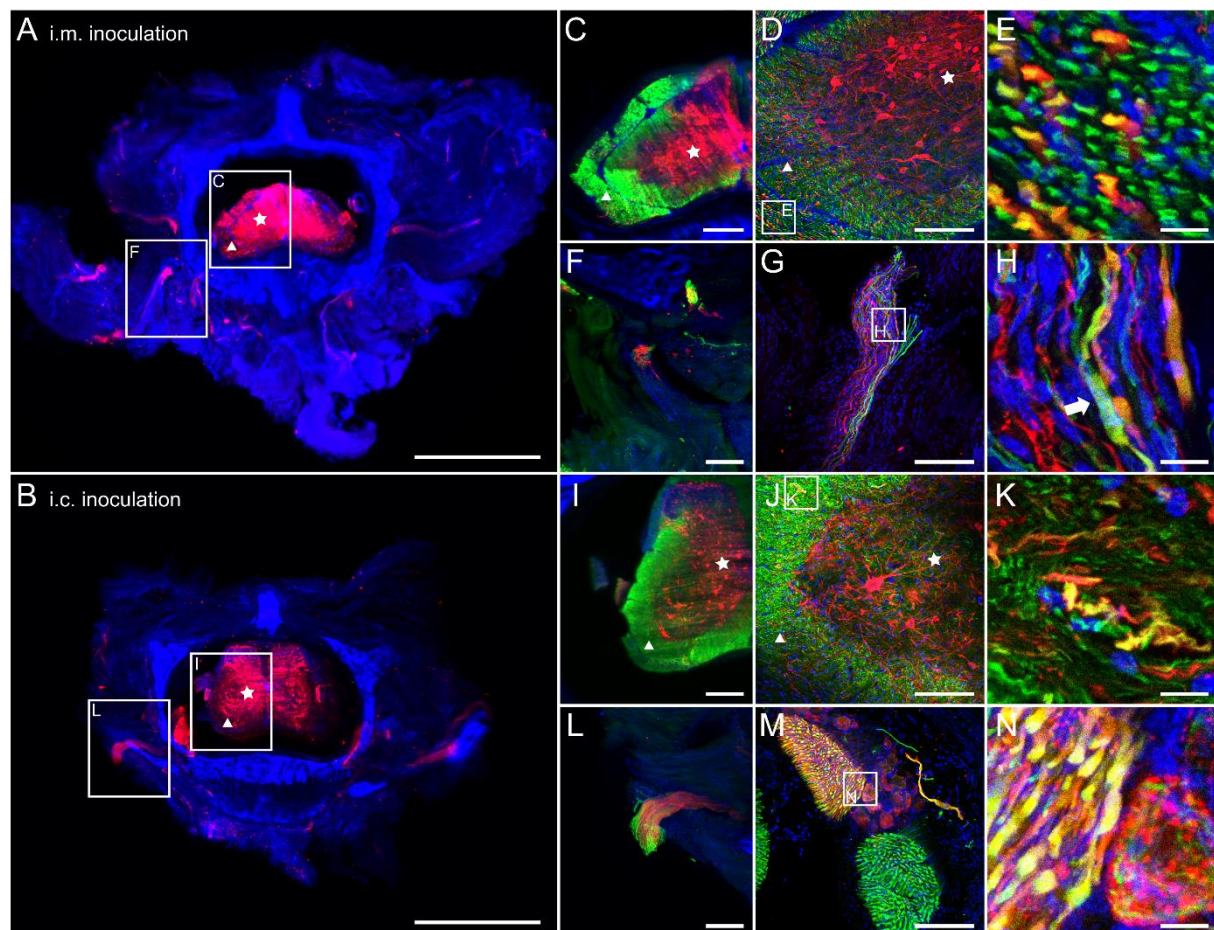
Fig. 4 Spinal column infection after i.m. and i.c. infection. (A,B) Maximum z-projections of light sheet overviews of cross sections of the spinal column after i.m. (A) and i.c. (B) infection [2.0x magnification; z = 824 µm (A), 1,480 µm (B)]. Red: RABV P; blue: nuclei. Green fluorescence for NEFM not shown as separation from green autofluorescence was not possible at low resolution. Stars: grey matter, triangles: white matter. Scale bar: 1,500 µm. **(C)** Maximum z-projection of detail from (A), including NEFM signals (green). Scale bar: 200 µm. **(D,E)** Maximum z-projection of confocal z-stacks of infected spinal cord (D) [z = 31 µm; Scale bar: 100 µm] and detail (E) [z = 10 µm; scale bar: 10 µm]. **(F)** Maximum z-projection of detail from (A) with neurons projecting from the spinal cord. Scale bar: 200 µm. **(G,H)** Maximum z-projection of confocal z-stacks (G) [z = 36 µm, Scale bar: 100 µm] and detail (H) [z = 10 µm; Scale bar: 10 µm] of projecting nerves from the spinal cord. **(I)** Maximum z-projection of detail from (B), including NEFM signals (green). Scale bar: 200 µm. **(J,K)** Maximum z-projection of confocal z-stacks of infected spinal cord (J) [z = 61 µm; Scale bar: 100 µm] and detail (K) [z = 20 µm; scale bar: 10 µm]. **(L)** Maximum z-projection of detail from (B), including NEFM signals (green). Scale bar: 200 µm. **(M,N)** Maximum z-projection of confocal z-stacks of projecting nerve (M) [z = 41 µm; Scale bar: 100 µm] and detail (N) [z = 20 µm; scale bar: 10 µm].
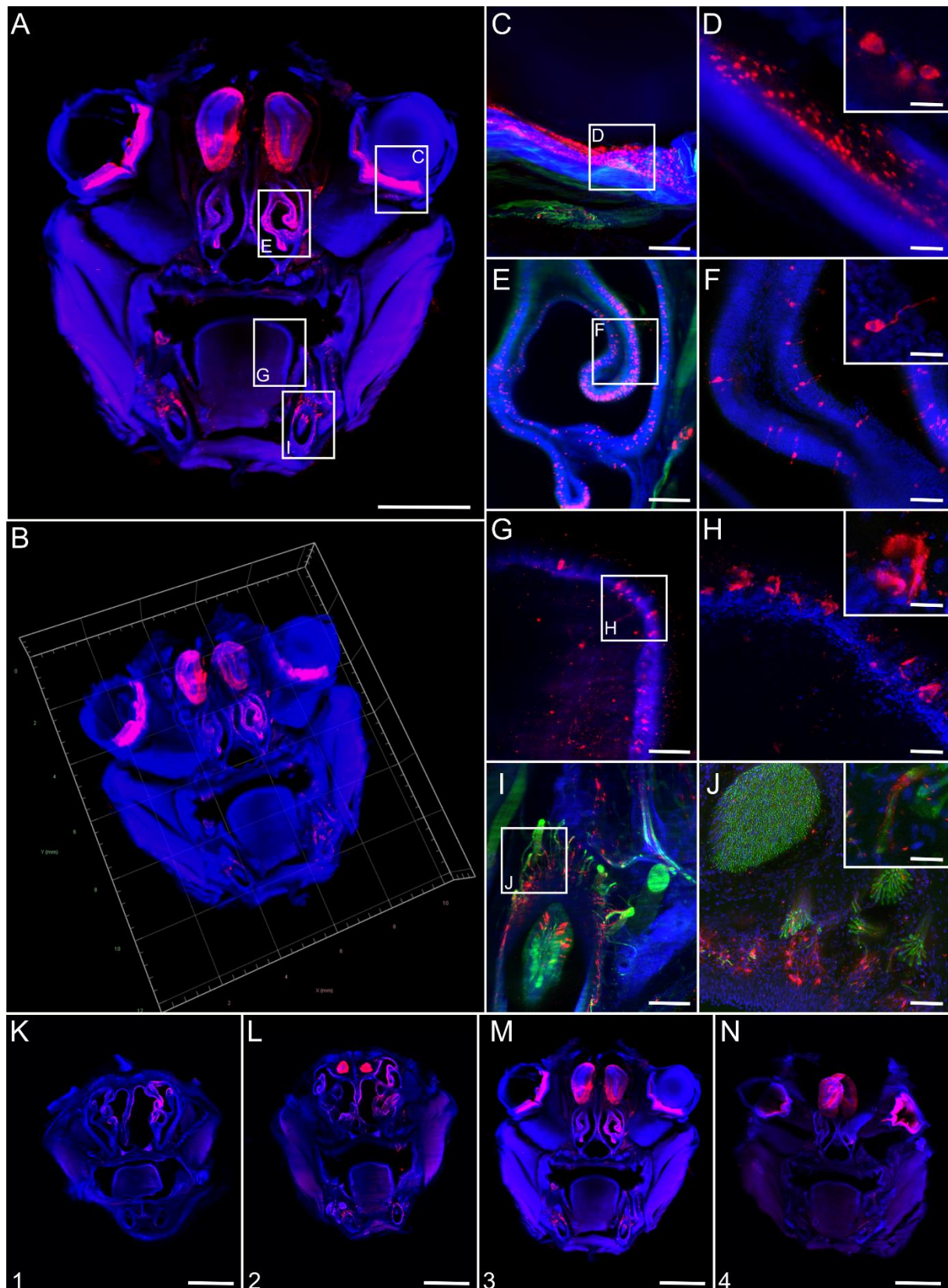
Fig. 5 Coronal overview of field RABV-infected mouse head sections after i.c. inoculation. **(A,B)** Maximum z- (A) and 3D projection (B) of mouse head sections after intracranial infection with field RABV [1.26x magnification; z = 1,606 µm]. Indirect immunofluorescence staining against RABV P (red), NEFM (green), and nuclei (blue). Green fluorescence for NEFM not shown as separation from green autofluorescence was not possible

28

610   at low resolution. Scale bar: 2,000 µm. **(C, E, G, I)** Maximum z-projections of details from A (white boxes) at a

611   magnification of 12.6x. Scale bar: 200 µm. **(D, F, H, J)** Confocal high-resolution z-stacks (corresponding to the

612   indicated regions in C, E, G, I, respectively) [z = 35 µm (D), 32 µm (F), 36 µm (H), 40µm (J); scale bar: 50 µm

613   and 15 µm in detail]. Note: due to the separate confocal image acquisition, the orientations differ from the light

614   sheet microscopy images in C, E, G, and I. **(C,D)** Infected eye, **(E, F)** nasal epithelium, **(G, H)** tongue, **(I, J)** and

615   teeth in mouse head coronal section. **(K-N)** Maximum z-projection of serial mouse head sections (Fig. S2B) [1.26x;

616   z = 1,780 µm (K), 1,820 µm (L), 1,606 µm (M), 1,760 µm (N); green not shown]. Scale bar: 2,000 µm.

617
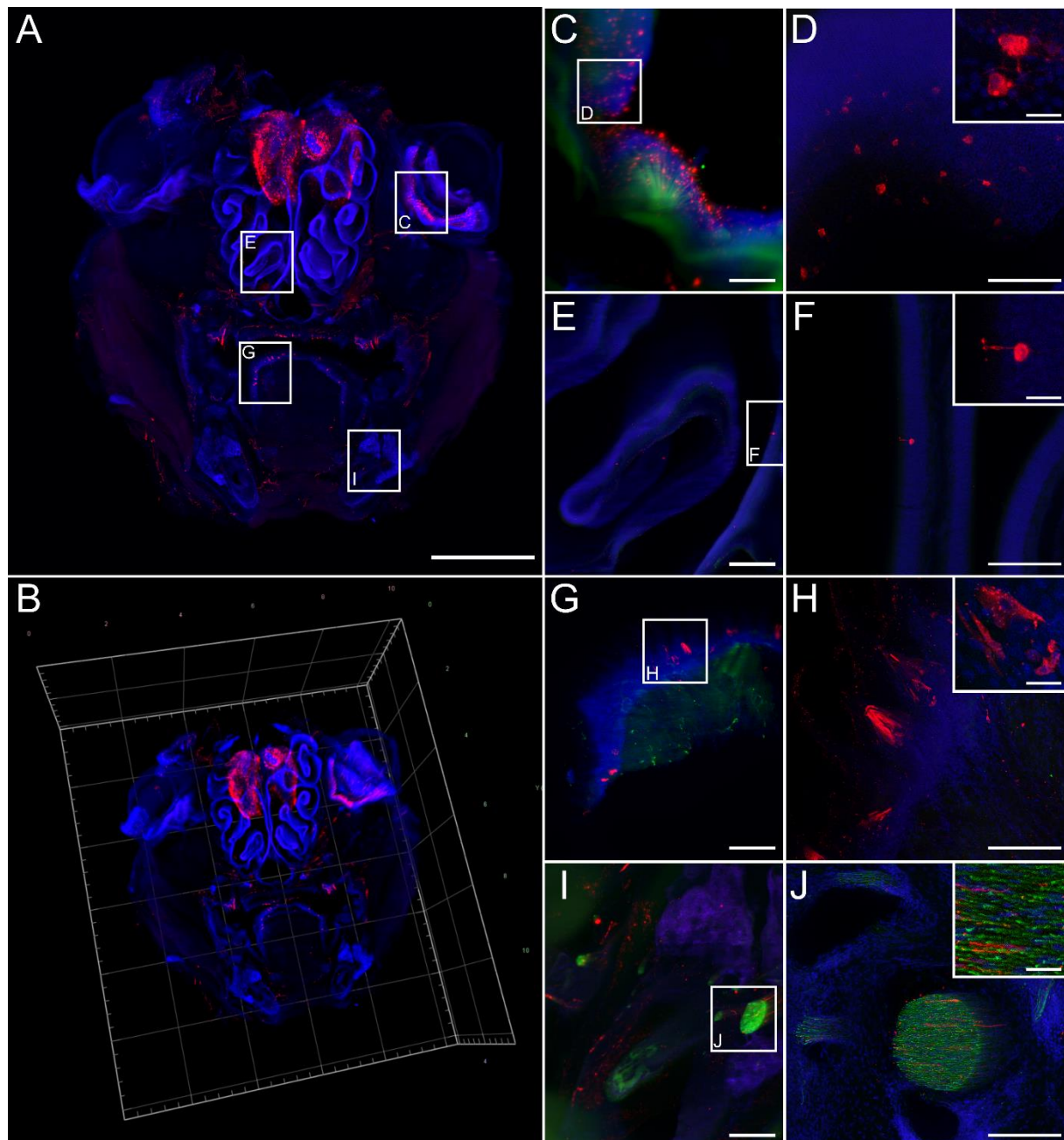
Fig. 6 RABV distribution in head cross sections after i.m. inoculation. **(A,B)** Maximum z- (A) and 3D projection (B) of coronal mouse head sections after i.m. infection with field RABV rRABV Dog [1.26x magnification; z = 4,210 µm]. Indirect immunofluorescence staining against RABV P (red), NEFM (green), and nuclei (blue) revealed a markedly reduced degree of infection after i.m. infection in comparison to i.c. infection (see Fig. 6). **(C, E, G, I)** Maximum z-projections of details from A (white boxes) [12.6x; magnification] (Scale bar: 200 µm). **(D, F, H, J)** Confocal high-resolution z-stacks (corresponding to **C, E, G, I**, respectively) [z = 80 µm (D), 26 µm (E), 72 µm (H), 74 µm (J); scale bar: 100 µm] with details (scale bar: 15 µm). **(C,D)** infected eye, **(E, F)** nasal epithelium, **(G, H)** tongue, **(I, J)** and teeth in mouse head coronal section.
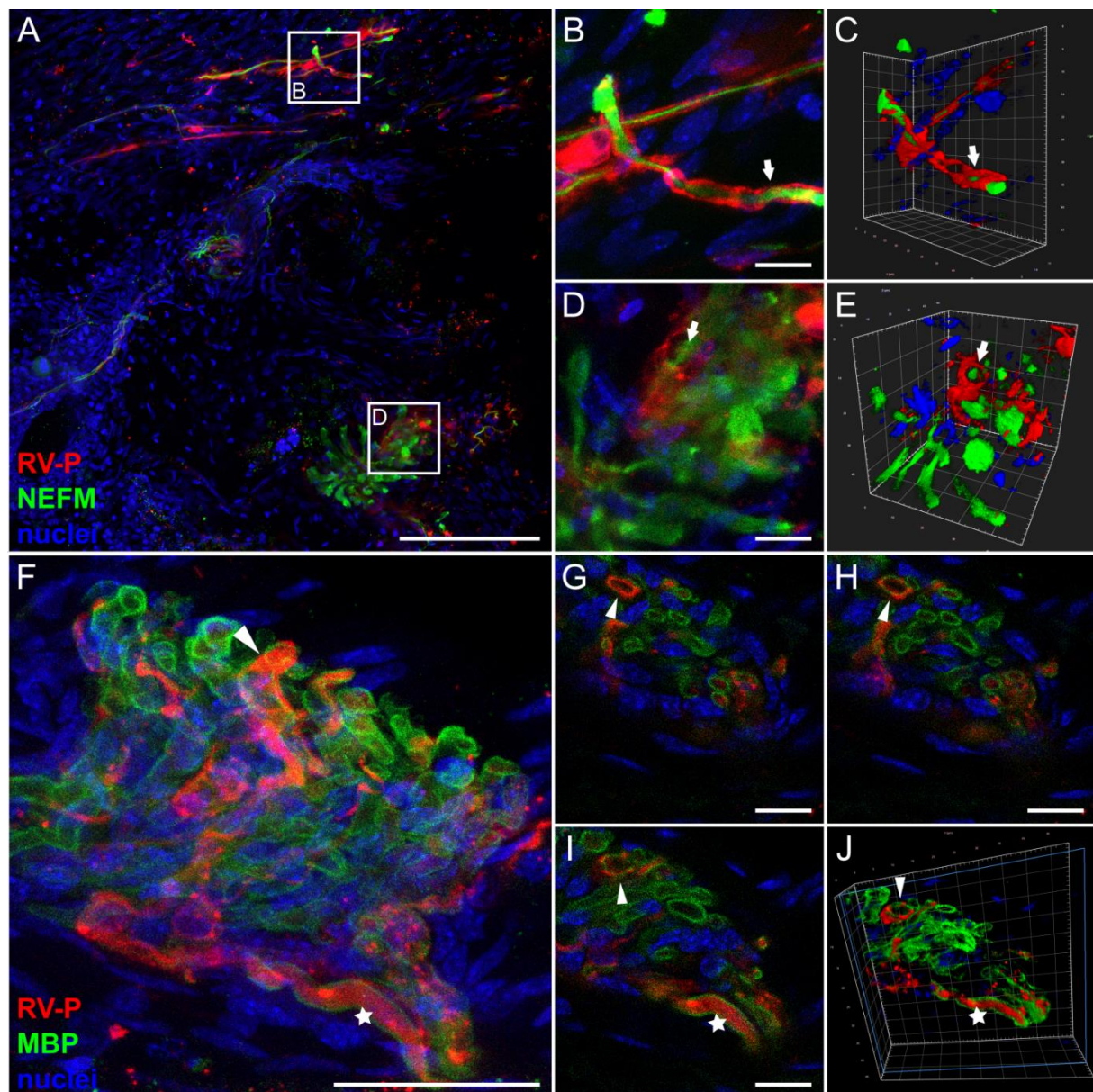
Fig 7 RABV P in axons and infected Schwann cells in coronal head sections. **(A)** Maximum z-projection of high-resolution confocal z-stacks of mouse head sections after i.c. inoculation and staining for RABV P (red), NEFM (green) and nuclei (blue) [z = 38 µm]. Arrows indicate RABV P surrounding NEFM. Scale bar: 100 µm. **(B-E)** Maximum z-projections (B, D) and corresponding 3D projections (C, E) of details of (A) (white boxes). **(F)** Maximum z-projection of confocal z-stacks of mouse head sections after i.c. inoculation stained for RABV P (red), MBP (green) and nuclei (blue) [z = 29 µm]. Scale bar: 25 µm. **(G-I)** Single slices of (F). Arrowhead: RABV P surrounding MBP-positive myelin sheath. Star: RABV P surrounded by MBP-positive myelin sheath. Scale bar: 5 µm. **(J)** 3D projection of (G-H).

Supplemantary Material

Supplementary Figures_S1-S6.pdf (including figure captions and descriptions)

Captions Videos S1-S7 (Captions and descriptions for supplementary videos)

Video S1.mp4

642   Video S2 reduced.avi

643   Video S3.mp4

644   Video S4.mp4

645   Video S5.mp4

646   Video S6.mp4

647   Video S7.avi

648

649

650

651